

# Vorticity moments in four numerical simulations of the 3D Navier–Stokes equations

Diego A. Donzis<sup>1</sup>, John D. Gibbon<sup>2</sup>†, Anupam Gupta<sup>3</sup>,  
Robert M. Kerr<sup>4</sup>, Rahul Pandit<sup>3,5</sup> AND Dario Vincenzi<sup>6</sup>

<sup>1</sup>Department of Aerospace Engineering, Texas A&M University,  
College Station, Texas, TX 77840, USA

<sup>2</sup>Department of Mathematics, Imperial College London, London SW7 2AZ, UK

<sup>3</sup>Department of Physics, Indian Institute of Science, Bangalore 560 012, India

<sup>4</sup>Department of Mathematics, University of Warwick, Coventry CV4 7AL, UK

<sup>5</sup>Jawaharlal Nehru Centre for Advanced Scientific Research, Bangalore, India

<sup>6</sup>Univ. Nice Sophia Antipolis, CNRS, LJAD, UMR 7351, 06100 Nice, France

(Received ?; revised ?; accepted ?. - To be entered by editorial office)

The issue of intermittency in numerical solutions of the 3D Navier–Stokes equations on a periodic box  $[0, L]^3$  is addressed through four sets of numerical simulations that calculate a new set of variables defined by  $D_m(t) = (\varpi_0^{-1} \Omega_m)^{\alpha_m}$  for  $1 \leq m \leq \infty$  where  $\alpha_m = \frac{2m}{4m-3}$  and  $[\Omega_m(t)]^{2m} = L^{-3} \int_V |\boldsymbol{\omega}|^{2m} dV$  with  $\varpi_0 = \nu L^{-2}$ . All four simulations unexpectedly show that the  $D_m$  are ordered for  $m = 1, \dots, 9$  such that  $D_{m+1} < D_m$ . Moreover, the  $D_m$  squeeze together such that  $D_{m+1}/D_m \nearrow 1$  as  $m$  increases. The values of  $D_1$  lie far above the values of the rest of the  $D_m$ , giving rise to a suggestion that a depletion of nonlinearity is occurring which could be the cause of Navier–Stokes regularity. The first simulation is of very anisotropic decaying turbulence; the second and third are of decaying isotropic turbulence from random initial conditions and forced isotropic turbulence at fixed Grashof number respectively; the fourth is of very high Reynolds number forced, stationary, isotropic turbulence at up to resolutions of  $4096^3$ .

## 1. Introduction

### 1.1. Background

Intermittency in both the vorticity and strain fields is a dominant feature of developing and developed turbulence. It has been studied extensively both experimentally (Sreenivasan 1985; Meneveau & Sreenivasan 1991) and numerically (Kerr 1985; Jimenez *et al.* 1993; Donzis, Yeung & Sreenivasan 2008; Ishihara, Gotoh & Kaneda 2009; Donzis & Yeung 2010; Donzis, Sreenivasan & Yeung 2012; Yeung, Donzis & Sreenivasan 2012). Statistical physicists generally use velocity structure functions to study this phenomenon and have diagnosed the degree of intermittency by measuring how much the order- $p$  velocity structure-function exponents  $\zeta_p$  differ from a simple linear dependence on  $p$  (Frisch 1995; Schumacher, Sreenivasan & Yakhot 2007; Boffetta, Mazzino & Vulpiani 2008; Pandit, Perlekar & Ray 2009). The standard way of quantifying equal-time, multi-scaling exponents is a challenging experimental and numerical task (Arneodo *et al.* 2008; Ray, Mitra & Pandit 2008; Ray *et al.* 2011). The multi-scaling approach is even more chal-

† Email address for correspondence: j.d.gibbon@ic.ac.uk

lenging for the three-dimensional (3D) Navier–Stokes equations

$$\partial_t \mathbf{u} + \mathbf{u} \cdot \nabla \mathbf{u} = \nu \Delta \mathbf{u} - \nabla P, \quad \operatorname{div} \mathbf{u} = 0, \quad (1.1)$$

because the velocity field  $\mathbf{u}(\mathbf{x}, t)$  and pressure  $P(\mathbf{x}, t)$  evolve in time, so, in general, time-dependent structure functions must be used to study dynamic multi-scaling (Ray *et al.* 2008, 2011). In this paper, we introduce a way of analysing some new, and existing, numerical computations; our analysis gives new insights into, and provides a new method for distinguishing between, alternative regimes of behaviour in the vorticity field. To explain the nature of these regimes, let us consider the vorticity field  $\boldsymbol{\omega} = \operatorname{curl} \mathbf{u}$  on a finite periodic domain  $\mathcal{V} = [0, L]^3$  within the setting of the volume integrals which define a set of frequencies

$$\Omega_m(t) = \left( L^{-3} \int_{\mathcal{V}} |\boldsymbol{\omega}|^{2m} dV \right)^{1/2m}, \quad 1 \leq m \leq \infty. \quad (1.2)$$

Some recent work has centred around a dimensionless re-scaling of the  $\Omega_m$  such that (Gibbon 2010, 2011, 2012a,b)

$$D_m(t) = (\varpi_0^{-1} \Omega_m)^{\alpha_m}, \quad \alpha_m = \frac{2m}{4m-3}, \quad (1.3)$$

where  $\varpi_0$  is a fixed frequency defined by  $\varpi_0 = \nu L^{-2}$ . (For the forced Navier–Stokes equations, definition (1.2) must be modified by adding  $\varpi_0$  to the integral term (Gibbon 2012a).) The origin of the above re-scaling, valid for both the Navier–Stokes and Euler equations, has been explained elsewhere (Gibbon 2011, 2012a,b) where it has been shown that, with additive  $L^2$ -forcing, weak solutions obey the time average up to time  $T$

$$\langle D_m \rangle_T \leq c Re^3 + O(T^{-1}). \quad (1.4)$$

The first in the hierarchy,  $D_1 = \varpi_0^{-2} Z$ , is proportional to the global enstrophy  $Z = \Omega_1^2$  and may be insensitive to deep fine-scale fluctuations. The higher  $D_m$  may be more sensitive so their measurement over a wide range of  $m$  could be a useful diagnostic of intermittency. However, the end of the sequence,  $D_\infty(t)$ , is hard to measure numerically, especially in highly intermittent flows. While Hölder’s inequality enforces a natural ordering on the frequencies  $\Omega_m$  such that  $\Omega_m \leq \Omega_{m+1}$  for  $1 \leq m \leq \infty$ , no such natural ordering is enforced on the  $D_m$  because the  $\alpha_m$  decrease with  $m$ . Thus there are two possible regimes:

$$D_{m+1}(t) < D_m(t), \quad (\text{regime I}), \quad D_m(t) \leq D_{m+1}(t), \quad (\text{regime II}). \quad (1.5)$$

The issues to be addressed in this paper in our four numerical simulations of the 3D Navier–Stokes equations are:

- (a) Which of these regimes is favoured or is there an oscillation between them? If one regime is favoured, are the  $D_m$  well separated? What is the role of the enstrophy  $D_1$ ?
- (b) Are these orderings  $m$ -dependent?
- (c) Are they  $Re$ -dependent?
- (d) Are they dependent upon initial conditions?

## 1.2. Simulations used for tests

An important point with respect to numerical simulations of the weighted higher order moments  $D_m(t)$  is that their ratios might converge better than their actual values. This is consistent with the results reported in Donzis *et al.* (2008), Yeung *et al.* (2012) and Donzis *et al.* (2012) where convergence for the ratios of higher-order vorticity and dissipation (strain) moments were obtained, even when the statistics of the individual

moments showed no evidence of convergence (Kerr 2012a). This answered a problem first raised in Kerr (1985) where it was noted that in forced simulations at modestly high Reynolds numbers, the averages of the vorticity and strain moments above 6-th order did not converge. The determination of the  $D_m(t)$  in simulations is not difficult whereas, in contrast, traditional numerical tools such as higher-order structure functions require a combination of larger domains and finer resolution than is currently feasible. In this paper, we calculate and compare the  $D_m(t)$  from four data sets: two in which the average kinetic energy  $E = L^{-3} \int_V \frac{1}{2} |\mathbf{u}|^2 dV$  decays in time, and two in which  $E$  is held approximately constant by forcing at the low wavenumbers. The first is a unique data set from a computation in which fully-developed turbulence forms from the interaction of two anti-parallel vortices and whose kinetic energy  $E$  decays strongly after the first peak in the normalised enstrophy production  $-S_u$  (Kerr 2013a). Some introductory discussion of this calculation is given in (§2). The other three data sets represent more traditional decaying and forced homogeneous, isotropic numerical turbulence. In the decaying calculations in §2 and the decaying and forced calculations in §3 the moments have been determined relatively continuously in time which makes a helpful comparison with the results of §1. For the fourth data set (comprising resolutions up to  $4096^3$ ) of §4, a similar conclusion is reached by studying the dependence of the time average of  $D_m$  on the Reynolds number. Inequality (1.4) is indeed uniform in  $m$  and, therefore, it is useful to study the behaviour of  $\langle D_m \rangle_T$  for different  $m$ , although this does not provide information on the pointwise-in-time ordering of the  $D_m$ .

An advantage of the first data set described in §2 is that the predicted convergence properties of ratios of the  $D_m(t)$  can be tested for a calculation with huge fluctuations in the production of enstrophy, and therefore in the higher  $D_m(t)$ . That the calculation eventually exhibits traditional turbulent statistics and spectra is a bonus in justifying its use. However, this new initial condition is very specialized and any trends need to be confirmed using a more traditional decaying homogeneous, isotropic data set, which is the purpose of the second calculation discussed in §3. Section 3 also contains forced simulations of homogeneous and isotropic turbulence at fixed Grashof number (a dimensionless measure of the ratio of the strength of the forcing term to that of the dissipative term — see, e.g., Doering & Gibbon (1995)). Finally, the fourth calculation in §4 studies the time average of  $D_m$  from a forced, massively parallel, pseudo-spectral calculation ( $4096^3$  with  $Re_\lambda \approx 1000$ ) to show that these trends are not restricted to low or moderate Reynolds numbers.

Assessing the scaling of moments of intermittent quantities such as vorticity, strain rates or velocity gradients has been a critical component of characterizing and understanding intermittency. Of particular interest is how these moments scale with the Reynolds number, which is typically high in applications. At the same time, different orders provide information about fluctuations of different intensities. Low and high-order moments, for example, are associated with weak and strong fluctuations. Thus, the understanding of the dependence of  $\langle D_m \rangle_T$  on  $Re$ , especially at high  $m$ , can also shed light on the nature of intermittency and the most extreme events in turbulence.

### 1.3. A summary of results

The simulations described in §2, §3 and §4, and illustrated in figures 2, 3, 4 and 7, each observe that a strict ordering occurs, as in regime I; namely  $D_{m+1}(t) < D_m(t)$  in §2 and §3 and  $\langle D_{m+1} \rangle_T < \langle D_m \rangle_T$  in §3 and in §4 (on log-linear plots). To assess the significance of this, we write down the relation  $D_{m+1} < D_m$  in terms of  $\Omega_m$  and use

Hölder's inequality  $\Omega_m \leq \Omega_{m+1}$  on the extreme left hand side

$$\varpi_0^{-1}\Omega_m \leq \varpi_0^{-1}\Omega_{m+1} < (\varpi_0^{-1}\Omega_m)^{\alpha_m/\alpha_{m+1}}. \quad (1.6)$$

As  $m \rightarrow \infty$ ,  $\alpha_m \searrow \alpha_{m+1}$ , and so (1.6) shows that  $\Omega_{m+1}/\Omega_m \searrow 1$ . Thus, in regime I the  $\Omega_m$  must be squeezed together for high  $m$ . In terms of the  $D_m$  (1.6) is written as

$$D_m^{\alpha_{m+1}/\alpha_m} \leq D_{m+1} < D_m. \quad (1.7)$$

While respecting the ordering  $D_{m+1} < D_m$ ,  $D_{m+1}$  is squeezed up close to  $D_m$  as  $m \rightarrow \infty$

$$\lim_{m \rightarrow \infty} \frac{D_{m+1}}{D_m} \nearrow 1. \quad (1.8)$$

This squeezing phenomenon is observed in all four data sets where the  $D_m$ -curves lie very close for  $m > 3$  as in figures 2, 3, 4 and 7. Moreover, the values of  $D_1$  in all four simulations lie far above the rest of the  $D_m$  giving rise to a suggestion, explored in §5, that a depletion of nonlinearity is occurring which could be the cause of Navier–Stokes regularity. The most extreme intermittent events are represented by moments at increasingly large  $m$ . Our results suggest the saturation of these high-order moments. This is significant as it constrains the shape of the tails of the probability density function (PDF) of vorticity which has been the focus of intense investigations (Kerr 1985; Jimenez *et al.* 1993; Donzis *et al.* 2008; Ishihara *et al.* 2009; Donzis & Yeung 2010; Yeung *et al.* 2012; Donzis *et al.* 2012). The fourth data set (forced, stationary, isotropic turbulence), the results of which are displayed in §4, furnishes us with the opportunity to compare these results with other results on intermittency available in the literature. For example, within the multifractal model, Nelkin (1990) found that normalized moments of velocity gradients scale as

$$\langle u_x^p \rangle / \langle u_x^2 \rangle^{p/2} \sim Re_\lambda^{d_p}, \quad (1.9)$$

where  $d_p$  is obtained from the multifractal spectrum and  $\langle \cdot \rangle$  is the usual notation for the statistical average (see also Schumacher, Sreenivasan & Yakhot 2007; Chakraborty, Frisch & Ray 2012). Using the well-known result  $\langle u_x^2 \rangle \sim (U_0/L)^2 Re_\lambda^2$  due to the dissipative anomaly, it is readily shown that  $\langle u_x^p \rangle \sim Re_\lambda^{p+d_p}$ . Our interest lies in the limit  $p \rightarrow \infty$  where it can be shown that  $\lim_{p \rightarrow \infty} d_p/p = c$ . The constant  $c$  is given by  $c = 3(1 - \mathcal{D}_\infty)/(3 + \mathcal{D}_\infty)$  with  $\mathcal{D}_\infty$  representing the limit  $\lim_{q \rightarrow \infty} \mathcal{D}_q$  of the generalized dimensions  $\mathcal{D}_q$  (Nelkin 1990; Hentschel & Procaccia 1983). Clearly, moments of the form  $\langle u_x^p \rangle^{1/p}$  saturate at high  $p$ , consistent with (1.8). Experimentally it is difficult to measure  $\mathcal{D}_\infty$  reliably; its value appears to be smaller than 1.0 (Meneveau & Sreenivasan 1991). One can further show that the ratio of successive orders is

$$\langle u_x^{p+1} \rangle^{1/(p+1)} / \langle u_x^p \rangle^{1/p} \sim Re_\lambda^{(1+d_p/p) - (1+d_{p+1}/(p+1))}. \quad (1.10)$$

The limiting behavior of  $d_p$  shows that  $\lim_{p \rightarrow \infty} [(1 + d_p/p) - (1 + d_{p+1}/(p+1))] = 0$ , and therefore the ratio on the left hand side of (1.10) tends to a constant independent of  $p$  and  $Re_\lambda$ . Although data on the multifractal characteristics of vorticity are limited, measurements (Meneveau *et al.* 1990) suggest an asymptotic value  $\mathcal{D}_\infty$  that is less than one, which is consistent with the unmistakable, but slow, squeezing together of  $\Omega_m$  and  $D_m$  as  $m$  increases.

## 2. The first set of simulations

A recent Navier-Stokes vortex reconnection calculation (Kerr 2013a), with an early time shown in figure 1a, has addressed the following long-standing numerical question:

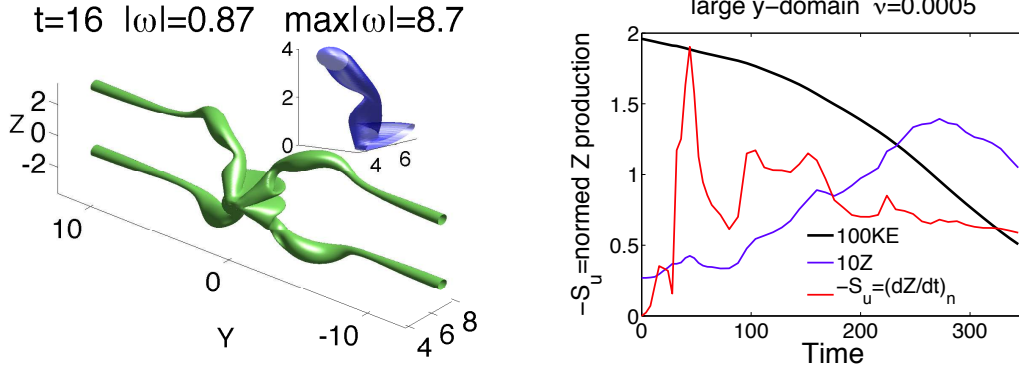


FIGURE 1. Figure 1a shows sosurfaces of the vorticity magnitude at  $t = 16$ . The initial condition is characterized by long anti-parallel vortices with a localized perturbation for the  $Re = 4000$  reconnection calculation. Figure 1b shows plots of the kinetic energy decay  $E$ , the enstrophy  $Z$  and its production, normalised to be consistent with experimental measurements of the velocity derivative skewness  $-S_u$ .  $Z$  grows until  $t \approx 270$  before falling, while  $E$  is always decaying.

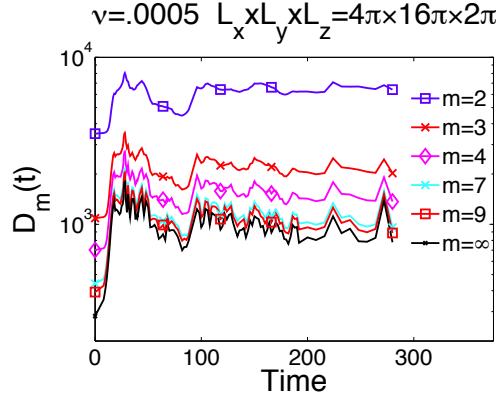


FIGURE 2.  $D_m$  curves ranging from  $m = 2$  and  $m = 9$  and including the normalised maximum of vorticity  $D_\infty$ . The normalized enstrophy,  $D_1$ , is far above the log scale given here, so is omitted. The  $D_m$  are ordered for all values of  $Re$  and all times.

Can a Navier-Stokes initial condition with only a few vortices generate and sustain fully-developed turbulence in a manner similar to how turbulence forms from the reconnection of anti-parallel vortices in aircraft wakes, or from the reconnection of quantum vortex lines and rings (Kerr 2011). This should include the formation of a high-wavenumber  $k^{-5/3}$  kinetic energy spectrum and additional diagnostics indicating that the energy is cascading to small scales. Kerr (2013a) has shown that the spectrum and supporting diagnostics are consistent with those in homogeneous turbulent flows and has suggested that the cascade is formed by the creation of a chain of swirling vortex rings through the reconnection of the original three-dimensional vortex structures.

Kerr (2013a) achieved this goal by using a new initial condition that was designed to address the shortcomings, described in Bustamante & Kerr (2008), of the Kerr (1993) initial condition. The two most important properties of the new initial condition are: (i) their initial profiles and directions should be balanced in the sense that they are neither internally unstable nor prone to the shedding of waves or vortex sheet formation; (ii) their initial perturbations need to be localized far from the periodic boundaries, twice as far as in any previous anti-parallel study. The calculation used an anisotropic mesh

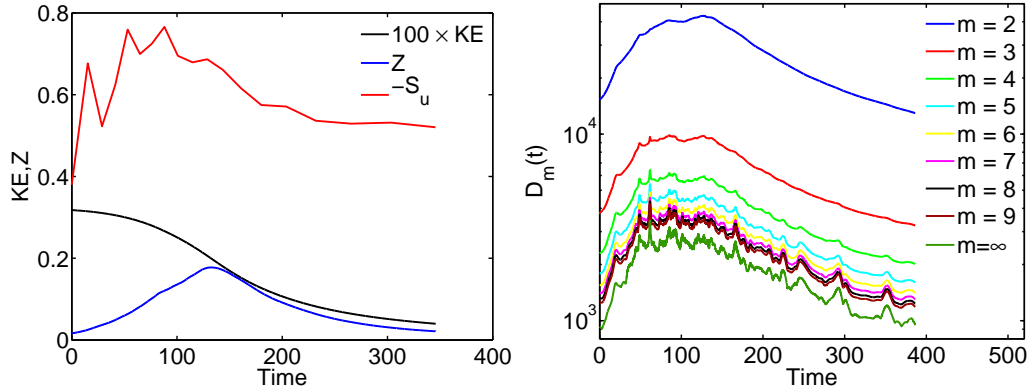


FIGURE 3. Figure 3a shows a plot versus time  $t$  of the total kinetic energy (black curve), the enstrophy  $Z$  (blue curve), the normalized enstrophy-production rate  $-S_u$  (red curve) for our DNS of decaying, 3D Navier-Stokes isotropic turbulence. Figure 3b is a plot of the  $D_m(t)$  for  $2 \leq m \leq 9$  (blue to brown curves) and  $D_\infty(t)$  (dark green curve) for decaying isotropic turbulence; the value of  $D_1$  is very high, so it is omitted. Zooming in to figure 3b makes it clear that  $D_{m+1}(t) < D_m(t)$  for all values of  $m$  considered and for all  $t$ .

of  $n_x \times n_y \times n_z = 512 \times 2048 \times 512$  in a  $L_x \times L_y \times L_z = 2\pi(2 \times 8 \times 1)$  domain, with symmetries applied to the  $y$  and  $z$  directions. The evolved state at the time of the first reconnection is shown in figure 1a.

In high-Reynolds number experiments and numerical simulations, the appearance of a persistent  $k^{-5/3}$  energy spectrum is commonly associated with the saturation of the normalised enstrophy production, which is usually written as the velocity derivative skewness  $S_u = \langle u_x^3 \rangle / \langle u_x^2 \rangle^{3/2}$ . Figure 1b shows a plot of  $-S_u$  versus time for the reconnection calculation; likewise figure 3a shows the equivalent for the decaying isotropic calculation of §3. The latest infinite  $Re$  estimates of  $S_u$  from forced turbulence calculations (Ishihara *et al.* 2009) have found  $-S_u \approx 0.68$ , consistent with experimental values of  $-S_u \sim 0.5 - 0.7$ . Early numerical calculations showed that the  $S_u$  tended to overshoot the early experimental values of  $-S_u \approx 0.4 - 0.5$  before settling to the expected value (Orszag & Patterson 1972). Both figures 1b and 3b confirm this trend, with  $-S_u$  rising above 0.6 before relaxing towards  $-S_u \approx 0.6$ .

In figure 2, note that all of the lower order  $D_m$  ( $m = 1, \dots, 9$ ) bound each higher-order  $D_m$  (on a log-scale), for all times, mirroring the major fluctuations in  $-S_u$ . This can be expressed as  $D_{m+1}(t) < D_m(t)$ , thus favouring regime I as in (1.5). The enstrophy  $D_1$  lies far above all of the other curves and has been omitted. Note the strong increase in the growth of each of the  $D_m$ , including  $D_\infty$ , up until  $t \approx 16$ . This is the period when this calculation has nearly Euler dynamics and the effects of viscosity compared to nonlinear growth are minimal. The growth of the  $D_m(t)$  in true Euler dynamics is the topic of another paper (Kerr 2013b).

### 3. The second and third sets of simulations: DNS results for homogeneous, isotropic turbulence

Data from two direct numerical simulations (DNSs) of homogeneous, isotropic 3D Navier-Stokes turbulence is now presented. Both of these simulations use a pseudospectral method, a 2/3-rule for de-aliasing, and  $512^3$  collocation points on a  $[0, 2\pi]^3$  domain. The first DNS is of decaying turbulence which reaches a Taylor-microscale Reynolds

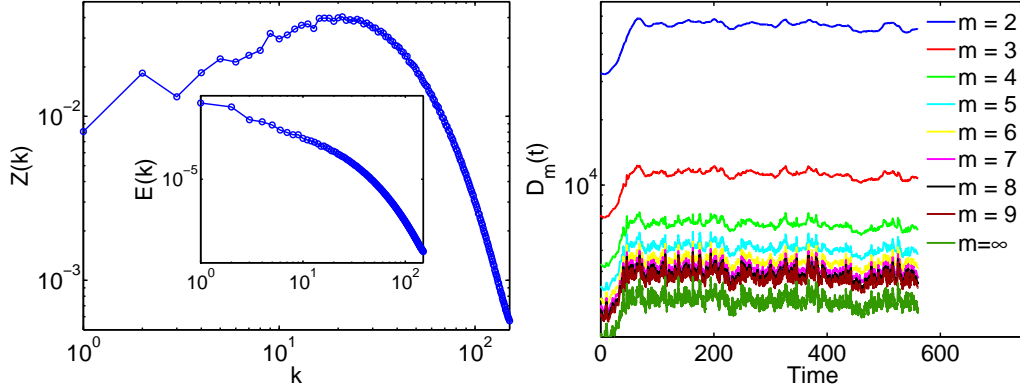


FIGURE 4. Figure 4a shows the enstrophy spectrum for statistically steady forced turbulence at  $Gr = 4.9 \times 10^7$ . The inset shows the kinetic-energy spectrum for the same simulation. Figure 4b shows the time series of  $D_m(t)$  for statistically steady forced turbulence at  $Gr = 4.9 \times 10^7$  ( $m = 1, \dots, 9$ ). Zooming in to the right panel makes it clear that  $D_{m+1}(t) < D_m(t)$  for all values of  $m$  considered and for all  $t$ .

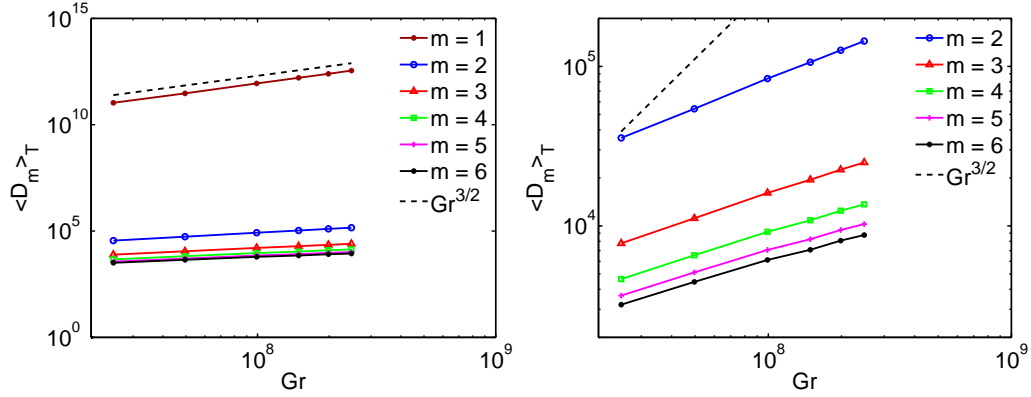


FIGURE 5. Figure 5a shows average values of  $D_m$  as a function of  $Gr$  for statistically steady forced turbulence at fixed Grashof number ( $m = 1, \dots, 6$ ). The dashed black line is  $Gr^{3/2}$ . The plot in figure 5b the same as figure 5a but on a different vertical scale with  $m = 2, \dots, 6$ .

number  $Re_\lambda \simeq 134$  at the main peak of the enstrophy  $Z$  associated with the formation of the inertial sub-range. The Taylor-microscale  $\lambda$  is defined in the usual way in terms of the energy spectrum  $E(k)$ . The initial Fourier components of the velocity  $\tilde{\mathbf{u}}_0(\mathbf{k})$  for the wave-vector  $k = |\mathbf{k}|$  are generated by applying random phases to the energy spectrum  $E_0(k) = E_0 k^4 \exp\{-2k^2\}$ . The kinematic viscosity is  $\nu = 5 \times 10^{-5}$ .

The second DNS is a study of statistically steady turbulence which attains  $Re_\lambda \simeq 182$ ; the forcing term  $\mathbf{f}_u(\mathbf{x}, t)$  is specified most simply in terms of  $\tilde{\mathbf{f}}_u(\mathbf{k}, t)$  whose spatial Fourier components are:

$$\tilde{\mathbf{f}}_u(\mathbf{k}, t) = \frac{\mathcal{P}\Theta(k_f - k)}{\sqrt{2E_u(k_f, t)}} \mathbf{u}(\mathbf{k}, t), \quad E_u(k_f, t) = \sum_{k \leq k_f} E(\mathbf{k}, t), \quad (3.1)$$

where  $\Theta$  is the Heaviside function and  $k_f = 2$  is the wave number above which Fourier modes are not forced. This forcing term maintains a constant Grashof number  $Gr = L^3 \mathcal{P} / \nu^2$  with  $L = 2\pi$ : for a similar forcing term that holds the energy injection fixed see Sahoo, Perlekar & Pandit (2011). The Grashof number is varied between  $2.48 \times 10^7$

---

$N^3$	$D_1$	$D_2$	$D_3$	$D_4$	$D_5$	$D_6$	$D_7$	$D_8$	$D_9$	$D_\infty$
$512^3$	$2.9268 \times 10^{11}$	54065.5	11088.3	6407.7	4924.3	4238.3	3853.4	3610.9	3445.7	2719.4
$256^3$	$2.9267 \times 10^{11}$	54062.8	11085.8	6404.7	4921.4	4235.9	3852.0	3610.4	3446.0	2623.3
$128^3$	$2.9288 \times 10^{11}$	54123.7	11149.7	6502.0	5045.7	4374.3	3994.4	3750.9	3581.5	2482.0

---

TABLE 1. Forced DNS at  $Gr = 4.9 \times 10^7$ : values of the  $D_m$  at  $t = 621$  (i.e., at the end of the simulation) calculated by using different numbers  $N^3$  of grid points.

---

$N^3$	$D_1$	$D_2$	$D_3$	$D_4$	$D_5$	$D_6$	$D_7$	$D_8$	$D_9$	$D_\infty$
$512^3$	$2.7714 \times 10^{10}$	24663.7	6138.6	3860.5	3122.4	2779.3	2586.3	2464.2	2381.7	1980.4
$256^3$	$2.7715 \times 10^{10}$	25667.9	6141.1	3862.4	3122.8	2777.2	2581.1	2456.0	2369.8	1980.4
$128^3$	$2.7683 \times 10^{10}$	24621.0	6103.0	3807.0	3051.0	2694.3	2491.0	2360.7	2270.5	1705.8

---

TABLE 2. Decaying DNS: values of the  $D_m$  at  $t = 128$  (i.e., at the peak of the enstrophy) calculated by using different numbers  $N^3$  of grid points.

and  $2.48 \times 10^8$  by changing  $\mathcal{P}$  while keeping  $\nu = 10^{-4}$  constant. For the decaying DNS, a small inertial subrange forms at  $t = 100$  when the enstrophy  $Z$  reaches its main peak. Assuming  $E(k) = K_0(k)\epsilon k^{-5/3}$ , the pre-factor  $K_0(k)$  is roughly 1.5 for about half a decade of wavenumbers. Similar to figure 1b, figure 3a shows the time-dependence of the kinetic energy  $E$ , enstrophy  $Z$  and its skewness  $-S_u$ . For the forced DNS at  $Gr = 4.9 \times 10^7$ , the energy and enstrophy spectra, in the statistically steady-state, are given in figure 4a. These spectra show that high-wave-number fluctuations of both the velocity and vorticity fields are well resolved in our simulation; the same holds for the other values of  $Gr$  considered.

Figures 3b and 4b show  $D_m(t)$  versus time  $t$  for  $m = 2, \dots, 9$  and  $D_\infty = (\varpi_0^{-1} \|\omega\|_\infty)^{\alpha_\infty}$  with  $\alpha_\infty = \frac{1}{2}$  for both the decaying and forced DNS calculations respectively. These plots show that  $D_m(t) < D_{m+1}(t)$  for all  $t$  and thus support the generality of figure 2 of §2.

The average values of  $D_m$ , as a function of  $Gr$ , are given in figure 5 for  $m = 1, \dots, 6$ . The behaviour of  $\langle D_m \rangle_T$  is consistent with the uniform bound  $\langle D_m \rangle_T \leq c_1 Gr^{3/2}$ , which can be obtained by combining (1.4) (Gibbon 2011) with the saturation of the bound  $Gr \leq c_2 Re^2$  (Doering & Foias 2002). Moreover, the average values of  $D_m$  satisfy  $\langle D_{m+1} \rangle_T < \langle D_m \rangle_T$  for all  $m$  and  $Gr$  considered, which is consistent with regime I.

A remark on the calculation of  $D_m$  concludes this section.  $D_m(t)$  is defined from the space integral of the  $2m$ -th power of  $\omega$  at time  $t$ . To compute  $D_m(t)$ , a sufficiently fine grid is required, especially if  $m$  is large. In our DNSs, the number of collocation points is  $512^3$ . The energy and enstrophy spectra given in figure 4a already show that small-scale fluctuations are sufficiently well resolved. However, to confirm that the resolution is sufficient, we have computed  $D_m(t)$  on a coarser grid by using only  $N^3$  of the  $512^3$



---

$N$	$Re_\lambda$	$k_{max}\eta$	Forcing
256	140	1.4	EP
256	140	1.4	FEK
512	140	2.7	FEK
2048	140	11.2	FEK
512	240	1.4	FEK
2048	240	5.1	FEK
1024	400	1.4	FEK
2048	400	2.8	EP
2048	650	1.4	EP
4096	650	2.7	FEK
4096	1000	1.3	FEK

---

TABLE 3. Parameters of statistically stationary forced simulations: included are the resolution  $N$ ,  $Re_\lambda$ , the resolution parameter  $k_{max}\eta$  and the forcing type (see text).

available grid points with  $N = 256, 128$ . We have repeated this calculation for some illustrative values of  $t$ . Our results show that the values of  $D_m$  (even for  $m = 9$ ) are reliable up to four or five significant figures. The difference between  $D_1$  and  $D_9$  appear at the level of the second significant figure. Thus, we conclude that  $D_{m+1}(t) < D_m(t)$  for all the values of  $m$  and  $t$  we have considered. Representative examples are given in tables 1 and 2. It is possible to infer from these tables that the calculation of  $D_m$  for much greater  $m$  would require an even higher resolution. Finally, in the calculation of  $\langle D_m \rangle_T$ , we have checked the convergence of the time average for all the  $m$  shown in figure 5 ( $m = 1, \dots, 6$ ).

#### 4. The fourth set of simulations: forced stationary isotropic turbulence

The DNS data in this fourth set of simulations were obtained using a massively parallel pseudo-spectral code which achieves excellent performance on  $O(10^5)$  processors. The basic numerical scheme is that of Rogallo (1981). The time stepping is second-order Runge–Kutta and the viscous term is exactly treated via an integrating factor. Aliasing errors are carefully controlled by a combination of truncation and phase shifting techniques. The database includes simulations with resolutions up to  $4096^3$  and Taylor-Reynolds number up to  $Re_\lambda \approx 1000$  (Donzis *et al.* 2012; Yeung *et al.* 2012). In order to maintain a stationary state, turbulence is forced numerically at the large scales. Since our objective here is to assess the generality of the ordering of the moments  $D_m$ , we show results using the stochastic forcing of Eswaran & Pope (1988) – denoted as EP – as well as a deterministic scheme described in Donzis & Yeung (2010) – denoted as FEK. In essence, this keeps the energy in the lowest wavenumbers fixed. For these two forcing schemes, the wavenumbers affected by forcing are confined to within a sphere  $k < k_F$ , where  $k_F$  is of order 2 or 3. In order to capture intense events, which are the main contributors to high-order moments, resolution issues have to be properly addressed. Motivated by the

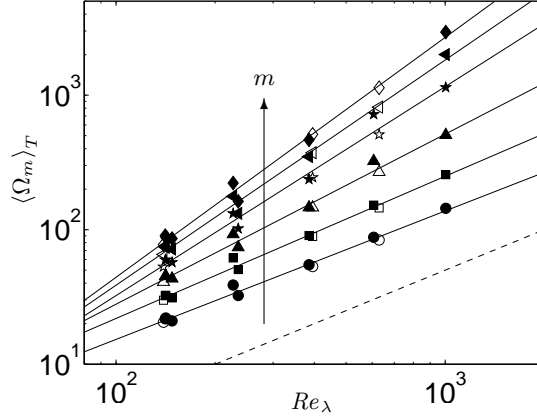


FIGURE 6. Scaling of  $\langle \Omega_m \rangle_T$  as a function of  $Re_\lambda$  for forced stationary isotropic turbulence with resolutions up to  $4096^3$ . Lines are for  $m = 1$  (circles), 2 (squares), 3 (triangles), 4 (stars), 5 (left triangles), 6 (diamonds). Open and closed symbols correspond to EP and FEK forcing respectively. Dashed line is  $\sim Re_\lambda^6$  (see text). Note that for  $Re_\lambda \approx 650$  at  $4096^3$  with FEK forcing, moments up to fourth order (instead of sixth) are available from our database.

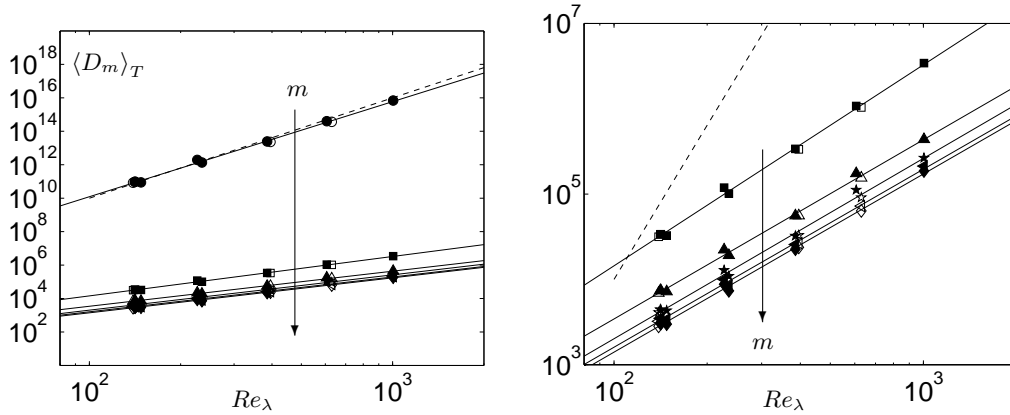


FIGURE 7. Scaling of  $\langle D_m \rangle_T$  and ratios as a function of  $Re_\lambda$  for forced stationary isotropic turbulence with resolutions up to  $4096^3$ . Figure 7a shows  $D_m$  versus  $Re_\lambda$  for  $m = 1$  to 6, while figure 7b is a zoom of figure 7a to highlight the ordering of  $\langle D_m \rangle_T$  for  $m = 2$  to 6. In both parts the dashed lines correspond to  $Re_\lambda^6$ .

theoretical work of Yakhot & Sreenivasan (2004), resolution effects have been studied in Donzis *et al.* (2008) and Yeung *et al.* (2012) with the conclusion that although high-order moments may be under-predicted using the standard resolution criterion – typically in simulations aimed at pushing up the Reynolds number – *ratios* of high-order moments are weakly affected by resolution issues. Small-scale resolution for a spectral simulation is typically quantified with the parameter  $k_{max}\eta$  where  $k_{max} = \sqrt{2}N/3$  is the highest resolvable wavenumber in a domain of size  $(2\pi)^3$  with  $N^3$  grid points. Simulations aimed at pushing the Reynolds number have typically used  $k_{max}\eta$  between 1 and 2. Here we present results from  $k_{max}\eta$  from the standard 1.5 up to 11, when available, which allows us to assess the effect of insufficient resolution. Table 3 summarizes those parameters of the DNS database that have been used.

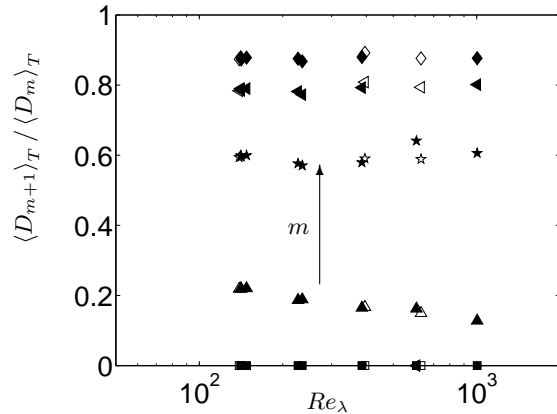


FIGURE 8. Ratio of moments  $\langle D_{m+1} \rangle_T / \langle D_m \rangle_T$  for  $m = 1$  (squares), 2 (triangles), 3 (stars), 4 (left triangles), and 5 (rhombi) as a function of  $Re_\lambda$ .

#### 4.1. The $D_m$ -moments in forced stationary isotropic turbulence

The time average of even moments of vorticity,  $\langle \Omega_m \rangle_T$ , are shown in figure 6. As assured by Hölder’s inequality it can be seen that  $\langle \Omega_{m+1} \rangle_T > \langle \Omega_m \rangle_T$  at all Reynolds numbers. Figure 6 also shows the line  $\sim Re_\lambda$  (dashed), which is the result of the dissipative anomaly. This is easily obtained from the kinematic relation  $\langle \epsilon \rangle = \nu \langle \Omega_1^2 \rangle_T$  associated with isotropic turbulence and the well-known scaling  $\langle \epsilon \rangle \sim U_0^3/L$ . It can then be shown that  $\langle \Omega_1 \rangle_T \sim (U_0/L)Re^{1/2} \sim (U_0/L)Re_\lambda$ , where the well-known result  $Re_\lambda^2 \sim Re$  has been used. The DNS data in figure 6 agree with this scaling. As mentioned above, some resolution effects can be expected especially for high orders. Where data at nominally the same Reynolds number but different resolution is available, moments tend to be higher for higher values of  $k_{max}\eta$  (Donzis *et al.* 2008). This is clearer at higher Reynolds number ( $Re_\lambda \approx 650$  where two resolutions are available). Ratios of moments, however, are only weakly affected by resolution, which is also consistent with more recent results (Donzis *et al.* 2008, 2012; Yeung *et al.* 2012). In figure 7, the time averages  $\langle D_m \rangle_T$  are shown as a function of  $Re_\lambda$ . For  $m = 1$ , one can again resort to using the dissipative anomaly with the definition  $D_1 = (\varpi_0^{-1}\Omega_1)^2$ . The result is

$$\langle D_1 \rangle_T = (L^2 \sqrt{\langle \epsilon \rangle} / \nu^{3/2})^2 \sim Re^3 \sim Re_\lambda^6 \quad (4.1)$$

which is seen in figure 7a. To see further details of higher order moments figure 7b does not include  $\langle D_1 \rangle_T$ . As in §2 and §3, the data clearly shows the ordering  $\langle D_{m+1} \rangle_T < \langle D_m \rangle_T$ . The insensitivity of the time averages of the moments to the type of forcing and the much weaker effect of resolution compared with  $\langle \Omega_m \rangle_T$  in figure 6 is also noted. The data also suggest that the ratio between the time averages of successive moments decreases with  $m$ , which is consistent with the asymptotic behaviour of equation (1.8). This is seen more clearly in figure 8, where the ratio of the time averages of successive moments,  $\langle D_{m+1} \rangle_T / \langle D_m \rangle_T$ , is plotted for different values of  $m$ . Consistent with an ordering  $\langle D_{m+1} \rangle_T < \langle D_m \rangle_T$ , the ratio is always less than unity. As  $m$  increases, however, this ratio becomes increasingly closer to unity in agreement with (1.8). It is also interesting that these ratios appear to be independent of Reynolds numbers which suggest a regime I ordering with clustering of moments at high  $m$  also in the high- $Re_\lambda$  limit. Resolution effects, while weak, can still be seen upon careful examination of the data, especially at high orders. However, for a given simulation, the ordering of regime I is unchanged with resolution.

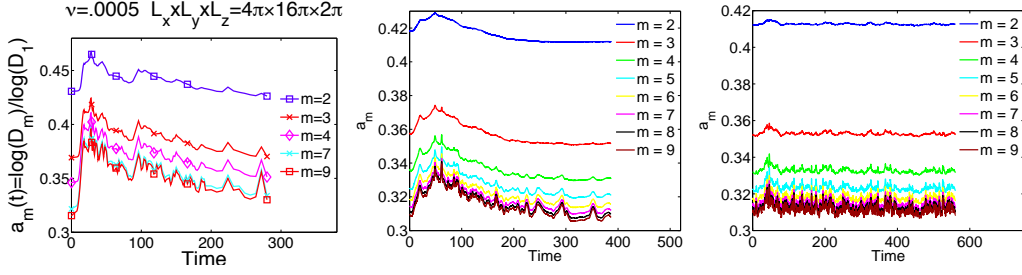


FIGURE 9. Plots of  $a_m$  for the three simulations in respectively §2 and §3 in which  $a_m < \frac{1}{2}$ : Figure 9a for the calculation in §2 and figures 9b and 9c for the decaying and forced calculations in §3.

## 5. Concluding remarks : the depletion of nonlinearity

The recent introduction of the  $D_m$ -vorticity-moment-scaling (Gibbon 2011, 2012a,b) motivated by the time average (1.4), has suggested that they should be applied to independent numerical simulations, such as the four data sets here. All four unexpectedly show that the  $D_m$  obey the ordering of regime I, namely  $D_{m+1} < D_m$ , which leads to the squeezing effect of (1.8) such that  $\Omega_{m+1}/\Omega_m \searrow 1$  and  $D_{m+1}/D_m \nearrow 1$  as  $m$  increases. This has an effect on the shapes of the PDF-tails, as remarked in §1.3. The ordering in the  $D_m$  is strict, even during intense events and, for  $m \geq 3, 4$ , the plots almost touch while replicating each other's shape, as in figures 2, 3b, 4b and 7b. It might be asked whether this is a viscous effect, a strictly nonlinear effect, or the result of some surprising symbiosis between the two? Using a variation of the anti-parallel initial condition used in §2, new Euler calculations have repeated this ordering over an extended period (Kerr 2013b), which implicates the nonlinear terms as the primary source. However, there is neither evidence from Navier-Stokes analysis that such an ordering should hold, nor do any results exist that suggest it cannot. It is, of course, possible that a cross-over could occur between regimes I and II at Reynolds numbers higher than have been achieved in this work, although figure 8 suggests otherwise.

Significantly  $D_1$  sits well above the other  $D_m$  and does not appear to converge with them during the most intense periods, which is why in figures 2, 3b, 4b and 7b the  $D_m$  are plotted on a log-scale with  $D_1$  omitted. We are therefore justified in writing

$$\ln D_m \lesssim a_m \ln D_1 \quad \Rightarrow \quad D_m \lesssim D_1^{a_m}. \quad (5.1)$$

Plots of  $a_m$  for the first and second pair of simulations are shown in figures 9a,b,c. Assuming a strong solution exists, the  $D_m$  have been shown to obey (see Gibbon 2012a)

$$\dot{D}_m \leq D_m^3 \left\{ -\varpi_{1,m} \left( \frac{D_{m+1}}{D_m} \right)^{\frac{2}{3}m(4m+1)} + \varpi_{2,m} \right\}, \quad (5.2)$$

where the  $c_{n,m}$  within  $\varpi_{1,m} = \varpi_0 \alpha_m c_{1,m}^{-1}$  and  $\varpi_{2,m} = \varpi_0 \alpha_m c_{2,m}$  are algebraically increasing with  $m$ . By dropping the negative term on the right hand side of (5.2), and replacing the  $D_m^3$ -term with  $D_m D_1^{2a_m}$  justified by (5.1), a time integration produces

$$D_m(t) \leq c_m \exp \int_0^t D_1^{2a_m} d\tau \leq c_m \exp \left\{ t^{1-2a_m} \left( \int_0^t D_1 d\tau \right)^{2a_m} \right\}, \quad 2a_m \leq 1. \quad (5.3)$$

Figures 9a,b,c show that while there is a weak dependence of  $a_m$  on both  $m$  and  $t$ , it nevertheless satisfies  $2a_m < 1$  in all cases. Leray's energy inequality insists that  $\int_0^t D_1 d\tau < \infty$

so it is clear that the right hand side of (5.3) is finite: *any* finite  $D_m$  is sufficient for Navier–Stokes regularity. This regularization can be traced to the *depletion of nonlinearity* in (5.1) in regime I. Although regime II has not been observed, (5.2) shows that it is associated with time-decay of the  $D_m$ . Specifically, if  $D_{m+1}/D_m \geq [c_{1,m}c_{2,m}]^{3/2m(4m+1)}$  then  $\dot{D}_m < 0$  where  $[c_{1,m}c_{2,m}]^{3/2m(4m+1)} \searrow 1$  for large  $m$ .

**Acknowledgements :** DD acknowledges the computing resources provided by the NSF-supported XSEDE and DOE INCITE programs under whose auspices some of these calculations were performed. RP and DV are members of the International Collaboration for Turbulence Research (ICTR). They acknowledge support from the ‘Indo-French Center for Applied Mathematics’, UMI IFCAM – Bangalore and, with RMK, the EU COST Action program MP0806 ‘Particles in Turbulence’. AG and RP thank DST, CSIR and UGC (India) and the SERC (IISC) for computational resources. JDG and RMK thank the Isaac Newton Institute, Cambridge, on whose programme *Topological dynamics in the Physical and Biological sciences (2012)* part of this work was carried out.

#### REFERENCES

- ARNEODO, A., BENZI, R., BERG, J., BIFERALE, L., BODENSCHATZ, E., BUSSE, A., CALZAVARINI, E., CASTAING, B., CENCINI, M., CHEVILLARD, L., FISHER, R. T., GRAUER, R., HOMANN, H., LAMB, D., LANOTTE, A. S., LEVEQUE, E., LUETHI, B., MANN, J., MORDANT, N., MUELLER, W.-C., OTT, S., OUELLETTE, N. T., PINTON, J.-F., POPE, S. B., ROUX, S. G., TOSCHI, F., XU, H. & YEUNG, P.K. 2008 Universal intermittent properties of particle trajectories in highly turbulent flows. *Phys. Rev. Lett.* **100**, 254504.
- BETCHOV, R. 1956 An inequality concerning the production of vorticity in isotropic turbulence. *J. Fluid Mech.* **1**, 497–504.
- BOFFETTA, G., MAZZINO, A. & VULPIANI, A. 2008 Twenty-five years of multifractals in fully developed turbulence: a tribute to Giovanni Paladin. *J. Phys. A: Math. Theor.* **41**, 363001.
- BUSTAMANTE, M. D. & KERR, R. M. 2008 3D Euler about a 2D symmetry plane. *Physica D* **237**, 1912–1920.
- CHAKRABORTY, S., FRISCH, U. & RAY, S.S. 2012 Nelkin scaling for the Burgers equation and the role of high-precision calculations. *Phys. Rev. E* **85**, 015301(R).
- DOERING, C. R. & GIBBON, J. D. 1995 *Applied analysis of the Navier–Stokes equations*. Cambridge University Press.
- DOERING, C. R. & FOIAS C. 2002 Energy dissipation in body-forced turbulence. *J. Fluid Mech.* **467**, 289–306.
- DONZIS, D., YEUNG, P. K. & SREENIVASAN, K. 2008 Dissipation and enstrophy in isotropic turbulence: scaling and resolution effects in direct numerical simulations. *Phys. Fluids* **20**, 045108.
- DONZIS, D. & YEUNG, P. K. 2010 Resolution effects and scaling in numerical simulations of passive scalar mixing in turbulence. *Physica D* **239**, 1278–1287.
- DONZIS, D., SREENIVASAN, K. & YEUNG, P. K. 2012 Some results on the Reynolds number scaling of pressure statistics in isotropic turbulence. *Physica D* **241**, 164–168.
- ESWARAN, V. & POPE, S. B. 1988 An examination of forcing in direct numerical simulations of turbulence. *Comput. Fluids* **16**, 257–278.
- FRISCH, U. 1995 *Turbulence: the legacy of A. N. Kolmogorov*, Cambridge University Press.
- GIBBON, J. D. 2010 Regularity and singularity in solutions of the three-dimensional Navier–Stokes equations *Proc. R. Soc. A* **466** 2587–2604.
- GIBBON, J. D. 2011 A hierarchy of length scales for weak solutions of the three-dimensional Navier–Stokes equations. *Comm. Math. Sci.* **10**, 131–136.
- GIBBON, J. D. 2012a Conditional regularity of solutions of the three dimensional Navier–Stokes equations and implications for intermittency. *J. Math. Phys.* **53**, 115608.
- GIBBON, J. D. 2012b Dynamics of scaled vorticity norms for the three-dimensional Navier–Stokes and Euler equations. arXiv:1212.0684. To appear in *Procedia IUTAM: Proceedings of IUTAM Symposium Topological Fluid Dynamics II* Cambridge.

- HENTSCHHEL, H. G. E. & PROCACCIA, I. 1983 The infinite number of generalized dimensions of fractals and strange attractors. *Physica D* **8**, 435–444.
- HOLM, D. D. & R. M. KERR, R. M. 2007 Helicity in the formation of turbulence. *Phys. Fluids* **19**, 025101.
- ISHIHARA, T., GOTOH T. & KANEDA, Y. 2009 Study of high-Reynolds number isotropic turbulence by direct numerical simulation. *Annu. Rev. Fluid Mech.* **41**, 16–180.
- JIMENEZ, J., WRAY, A., SAFFMAN, P. G. & ROGALLO, R. S. 1993 The structure of intense vorticity in isotropic turbulence. *J. Fluid Mech.* **255**, 65–90.
- KERR, R. M. 1985 Higher-order derivative correlations and the alignment of small-scale structures in isotropic numerical turbulence. *J. Fluid Mech.* **153**, 31–58.
- KERR, R. M. 1993 Evidence for a singularity of the three-dimensional incompressible Euler equations. *Phys. Fluids A* **5**, 1725–1746.
- KERR, R. M. 2011 Vortex stretching as a mechanism for quantum kinetic energy decay. *Phys. Rev. Lett.* **106**, 224501.
- KERR, R. M. 2012a Dissipation and enstrophy statistics in turbulence: Are the simulations and mathematics converging? *J. Fluid Mech.* **700**, 1–4.
- KERR, R. M. 2012b Bounds on a singular attractor in Euler using vorticity moments, <http://arxiv.org/abs/1212.1106>, to appear in *Procedia IUTAM, Proceedings of IUTAM Symposium Topological Fluid Dynamics II* Cambridge.
- KERR, R. M. 2013a Swirling, turbulent vortex rings formed from a chain reaction of reconnection events. *Phys. Fluids* **25**, 065101.
- KERR, R. M. 2013b Bounds for Euler from vorticity moments and line divergence *J. Fluid Mech.*, in press.
- MENEVEAU, C., SREENIVASAN, K. R., KAILASNATH, P. & FAN, M. S. 1990 Joint multifractal measures: Theory and applications to turbulence. *Phys. Rev. A* **41**, 894–913.
- MENEVEAU, C. & SREENIVASAN, K. R. 1991 The multifractal nature of turbulent energy dissipation. *J. Fluid Mech.* **224**, 429–484.
- NELKIN, M. 1990 Multifractal scaling of velocity derivatives in turbulence. *Phys. Rev. A* **42**, 7226–7229.
- ORSZAG, S. A. & PATTERSON, G. S. 1972 Numerical simulation of three-dimensional homogeneous isotropic turbulence. *Phys. Rev. Lett.* **28**, 76–79.
- PANDIT, R., PERLEKAR, P. & RAY, S. S. 2009 Statistical properties of turbulence: An overview, *Pramana – Journal of Physics* **73**, 157–191.
- RAY, S. S., MITRA, D. & PANDIT, R. 2008 The universality of dynamic multiscaling in homogeneous, isotropic Navier–Stokes and passive-scalar turbulence. *New J. Phys.* **10**, 033003.
- RAY, S. S., MITRA, D., PERLEKAR, P. & PANDIT, R. 2011 Dynamic multiscaling in two-dimensional fluid turbulence. *Phys. Rev. Lett.* **107**, 184503.
- ROGALLO, R. S. 1981 Numerical experiments in homogeneous turbulence. *Tech. Rep.* 81835. NASA Tech. Mem.
- SAHOO, G., PERLEKAR, P. & PANDIT, R. 2011 Systematics of the magnetic-Prandtl-number dependence of homogeneous, isotropic magnetohydrodynamic turbulence. *New J. Phys.* **13**, 013036.
- SCHUMACHER, J., SREENIVASAN, K. R. & YAKHOT, V. 2007 Asymptotic exponents from low-Reynolds-number flows. *New J. Phys.* **9**, 89–107.
- SREENIVASAN, K. R. 1985 On the fine-scale intermittency of turbulence. *J. Fluid Mech.* **151**, 81–103.
- YAKHOT, V. & SREENIVASAN, K. R. 2004 Towards a dynamical theory of multifractals in turbulence. *Physica A* **343**, 147–155.
- YEUNG, P. K., DONZIS, D. & SREENIVASAN, K. R. 2012 Dissipation, enstrophy and pressure statistics in turbulence simulations at high Reynolds numbers. *J. Fluid Mech.* **700**, 5–15.